

SPECIAL ISSUE PAPER

SNR and throughput analysis of distributed collaborative beamforming in locally-scattered environments

Slim Zaidi* and Sofiène Affes

INRS-EMT, Montreal, Quebec, Canada

ABSTRACT

Three main collaborative beamforming (CB) solutions based on different channel models exist: the optimal CSI-based CB (OCB), the conventional or monochromatic (i.e., single-ray) distributed CB (M-DCB), and the recently developed bichromatic (i.e., two-ray) distributed CB (B-DCB). In this paper, we perform an analytical comparison, under practical constraints, between these CB solutions in terms of achieved signal-to-noise ratio (SNR) as well as achieved throughput. Assuming the presence of local scattering in the source vicinity and accounting for implementation errors incurred by each CB solution, we derive for the first time closed-form expressions of their true achieved SNRs. For low angular spread (AS), where both solutions nominally achieve the same SNR in ideal conditions, we show that the B-DCB always outperforms OCB, more so and at larger regions of AS values when errors increase. Excluding exceptional circumstances of unrealistic low quantization levels (i.e., very large quantization errors) that are hard to justify in practice, we also show that the new B-DCB always outperforms the M-DCB as recently found nominally in ideal conditions. This work is also the first to push the performance analysis of CB to the throughput level by taking into account the feedback overhead cost incurred by each solution. We prove both by concordant analysis and simulations that the B-DCB is able to outperform, even for high AS values, the OCB which is penalized by its prohibitive implementation overhead, especially for a large number of collaborating terminals and/or high Doppler frequencies. Indeed, it is shown that the operational regions in terms of AS values over which the new B-DCB is favored against OCB in terms of achieved throughput can reach up to 40°. Copyright © 2012 John Wiley & Sons, Ltd.

KEYWORDS

distributed collaborative beamforming; local scattering; angular distribution/spread; monochromatic/single-ray; multi-ray channels; bichromatic/two-ray approach; throughput analysis; wireless sensor networks

*Correspondence

Slim Zaidi, INRS-EMT, Montreal, Quebec, Canada.

E-mail: zaidi@emt.inrs.ca

1. INTRODUCTION AND BACKGROUND

In wireless communication, transmit (Tx) or receive (Rx) beamforming refers to a technique in which a multiple-antenna transceiver transmits or receives a message through its K antennas [1–14]. Each antenna multiplies its Tx or Rx signal by a beamforming weight so that signals are constructively combined at the destination. Several approaches can be adopted to properly select these weights such as minimizing the total transmit power subject to the received quality-of-service constraint, maximizing the received signal-to-noise ratio (SNR) subject to the total transmit power constraint, or simply matching the channel between the source or receiver and each antenna [1,2]. In this work, we are particularly interested in

minimizing the noise power while keeping the beamformer response in the desired direction equal to unity (i.e., distortionless response). When the beamforming response in the desired direction is fixed, it has been shown that the Tx or Rx beamforming technique is able to achieve a K -fold gain against single-antenna communication schemes in both received SNR and power efficiency (i.e., a K -fold decrease in the antennas power consumption) [1–5]. However, when practical constraints (size constraint, etc.) rule out the use of multiple-antenna units, a collaborative communication scheme among K single-antenna small-battery-powered terminals called Tx or Rx collaborative beamforming (CB) can alternatively be used to emulate conventional beamforming [6–14]. Because of the very often stringent limitation in battery power available at each collaborative terminal, it is of utmost importance that CB

techniques be power efficient. A distinguishing feature of CB with respect to conventional beamforming is that terminals are often located at different physical locations, are wireless connected, and have independent local clocks and oscillators. Hence, any collaborative scheme to be devised and implemented among the CB terminals would necessarily require some degree of communication between them, an inevitable overhead that has to be minimized to avoid depleting battery power and useful throughput.

One such collaborative scheme is prerequisite synchronization in frequency, phase, and time between terminals prior to CB itself to allow them operate virtually as a single physical entity. Indeed, in order to avoid destructive combining of signals at the destination, which would be catastrophic for CB, terminals must synchronize their carrier frequencies and transmit their corresponding signal at the same time. To address this challenge, different research groups developed synchronization approaches that are power, cost, and spectrum efficient, such as those in [7–10]. Another equally important challenge is the CB design itself once prerequisite synchronization is achieved as assumed in this work. An important issue in CB design is that terminals are autonomous units that have limited knowledge about each other in the network. In the very likely event where the designed weights would depend on the locally unavailable information at every terminal, the latter would not be able to compute its own weight without severely depleting throughput and power from the huge overhead potentially requested [11–14]. To get around this problem, a master terminal with global knowledge of the network is envisaged to compute, as appropriate, all weights or all required channel state information (CSI) and broadcast them to the terminals [11,12]. Commonly known as centralized CB, the implementation overhead of this scheme increases proportionally to K and becomes prohibitive especially when the number of terminals is typically large such as those in wireless sensor networks. This impediment motivates further investigation of more power-efficient and spectrum-efficient CB techniques.

In [13] and [14], lending themselves to a distributed implementation, the authors proposed a variety of so-called distributed CB (DCB) techniques wherein the designed weights solely depend on the information commonly available at every terminal, and hence, each terminal is able to locally compute its own weight. So far, however, such works neglected the scattering and reflection effects and assumed plane-wave (single-ray) propagation channels termed here as monochromatic (with reference to their angular distribution). By fitting the true channel into an array manifold that is mainly parameterized by the source position, this assumption allows a distributed implementation by ridding each CB weight at large K from any information locally unavailable [13,14]. However, this assumption is only valid in far-field line-of-sight environments with very low scattering that, apart from rural areas, are not valid in urban or even suburban macro-cell areas. Indeed, in such environments, the presence of

local scattering in the receiver (source) vicinity causes an angular spread (AS) of the Rx or Tx signal. Hence, L independent and identically distributed (i.i.d.) rays or ‘spatial chromatics’ (with reference to their angular distribution) arise to form a multi-ray (L -ray) channel [15–18]. Because of the resulting mismatch in the expected distortionless response between the nominal single-ray and the true multi-ray channels, it was shown in [16] that the performance of monochromatic DCB (M-DCB) techniques degrades in rural areas where the AS is still very small and becomes unsatisfactory when the AS increases such as in suburban and urban areas. This impediment unfortunately limits the DCB’s real-world applicability range. It is noteworthy that the CSI-based centralized CB schemes discussed earlier could properly handle multi-ray channel environments and implement optimal distortionless CB (OCB), but again, the overhead associated with the K channel estimations would be prohibitive, especially when K is large and/or when estimates have to be frequently updated at high Doppler [19–23]. In [24] and [25], we have recently developed a new CB design that combines the benefits of M-DCB (i.e., small-overhead-distributed implementation) and OCB (i.e., better match with the true channel in scattered environments) and which avoids their respective drawbacks (channel mismatch and large overhead). Exploiting the fact that for low AS, a multi-ray channel—owing to a Taylor series expansion of its correlation matrix—can be properly approximated by two angular rays and hence considered as bichromatic, we developed a new bichromatic DCB (B-DCB). In [25], we analyzed and compared the B-DCB against M-DCB in terms of SNR performance without accounting for implementation errors (i.e., in ideal conditions). We showed that the B-DCB solution always outperforms its M-DCB vis-a-vis and is able to achieve until 3 dB of average-signal-to-average-noise ratio (ASANR) gains.

In this work, we consider for analysis not only the M-DCB and the B-DCB but also the OCB solution to achieve a dual-hop communication from a source to a receiver, through a wireless network comprised of K independent terminals. Assuming the presence of local scattering in the source vicinity and accounting for estimation and quantization errors incurred by each CB solution, we compare their achieved SNRs in practical conditions. To this end, we derive for the first time their true achieved SNRs in closed-form taking into account estimation and feedback quantization errors. For low AS, where both solutions nominally achieve the same SNR in ideal conditions, we show that B-DCB always outperforms OCB, more so at larger regions of AS values when errors increase. Excluding exceptional circumstances of unrealistic low quantization levels (i.e., very large quantization errors) hard to justify in practice, we also show that the new B-DCB always outperforms the M-DCB as recently found nominally in ideal conditions. This work is also the first to push the performance analysis of CB to the throughput level by taking into account the feedback overhead cost incurred by each

solution. We prove both by concordant analysis and simulations that the B-DCB is able to outperform, even for high AS values, the OCB, which is penalized by its prohibitive implementation overhead, especially for a large number of collaborating terminals and/or high Doppler frequencies. Indeed, it is shown that the operational regions in terms of AS values over which the new B-DCB is favored against OCB in terms of achieved throughput can reach up to 40°.

The rest of this paper is organized as follows. The system model is described in Section 2. The CB techniques in the presence of local scattering are presented in Section 3. Section 4 compares the performance of these techniques in terms of ASANR, whereas Section 5 compares them in terms of the link-level throughput. Simulations results are shown in Section 6 and concluding remarks are given in Section 7.

Notation: Uppercase and lowercase bold letters denote matrices and vectors, respectively. $[·]_{il}$ and $[·]_i$ are the (i, l) th entry of a matrix and i th entry of a vector, respectively. \mathbf{I} is the identity matrix and \mathbf{e}_l is a vector with one in the l th position and zeros elsewhere. $(·)^T$ and $(·)^H$ denote the transpose and the Hermitian transpose, respectively. $\|·\|$ is the two-norm of a vector, and $|·|$ is the absolute value. $E\{·\}$ stands for the statistical expectation, and $\left(\xrightarrow{ep1}\right) \xrightarrow{p1}$ denotes (element-wise) convergence with probability one. $J_1(·)$ is the first-order Bessel function of the first kind and \odot is the element-wise product.

2. SYSTEM MODEL

As can be observed from Figure 1, in this work, both Rx and Tx CB schemes are of concern. As illustrated in Figure 1(a), the system of interest in the Rx CB configuration consists of a wireless network or subnetwork comprised of K uniformly and independently distributed terminals on $D(O, R)$, the disc with center at O and radius R , a receiver at O , and a source S located in the same plane containing $D(O, R)$ [4,5,13]. We assume that there is no direct link from the source to the receiver because of pathloss attenuation. Moreover, let (r_k, ψ_k) denote the polar coordinates of the k th terminal and (A_s, ϕ_s) denote those of the source. Without loss of generality, the latter is assumed to be at $\phi_s = 0$ and to be located in the far-field region; hence, $A_s \gg R$. In a dual-hop communication scheme, each terminal receives the desired signal from the source in the first hop, then multiplies it by a properly designed CB weight and forwards the resulting signal to the receiver in the second hop. Description of the Tx CB configuration in Figure 1(b) is straightforward from the previous, where only the source and receiver switch positions.

The following assumptions are further considered with respect to the Rx CB configuration in Figure 1(a) or the Tx CB configuration in Figure 1(b):

- (A1) The far-field source or receiver is scattered by a large number of scatterers within its vicinity. The latter generates from the Tx or Rx signal

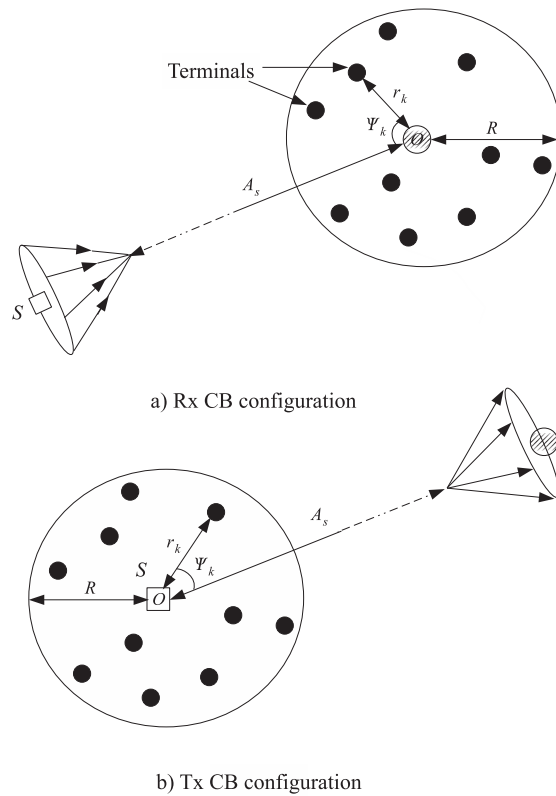


Figure 1. Rx and Tx system configurations.

L equal-power rays or ‘spatial chromatics’ (with reference to their angular distribution) that form an L -ray propagation channel [15–18]. The l th ray or chromatic is characterized by its angle θ_l and its complex amplitude $\alpha_l = \rho_l e^{j\xi_l}$ where the amplitudes $\rho_l, l = 1, \dots, L$, and the phases $\xi_l, l = 1, \dots, L$, are i.i.d. random variables, and each phase is uniformly distributed over $[-\pi, \pi]$. The angles $\theta_l, l = 1, \dots, L$, are also i.i.d. random variables with variance σ_θ^2 and probability density function $p(\theta)$ [16–18]. All θ_l s, ξ_l s, and ρ_l s are mutually independent. Note that the standard deviation σ_θ is commonly known as the AS whereas $p(\theta)$ is called the scattering or angular distribution.

- (A2) The channel gain $[\mathbf{f}]_k$ between the k th terminal and the receiver, or the source is a zero-mean unit-variance circular Gaussian random variable [13].
- (A3) The source signal s is a zero-mean random variable with power p_s , whereas noises at terminals and the receiver are zero-mean Gaussian random variables with variances σ_v^2 and σ_n^2 , respectively. The source signal, noises, and the terminals forward or backward channel gains are mutually independent.
- (A4) The k th terminal is aware of its own coordinates (r_k, ψ_k) , its forward or backward channel $[\mathbf{f}]_k$, the directions of the source ϕ_s, K , and σ_θ^2 while

being oblivious to the locations and the forward and backward channels of *all* other terminals in the network.

Using A1 and the fact that $A_s \gg R$, the channel gain between the k th terminal and the source or the receiver can be represented as

$$[\mathbf{g}]_k = \sum_{l=1}^L \alpha_l e^{-j \frac{2\pi}{\lambda} r_k \cos(\theta_l - \psi_k)} \quad (1)$$

where λ is the wavelength.

3. CB TECHNIQUES IN THE PRESENCE OF LOCAL SCATTERING

3.1. Rx CB configuration

In this scheme, a dual-hop communication is established from the source S to the receiver. In the first time slot, the source sends its signal s to the wireless network. Let \mathbf{y} denote the received signal vector at the terminals given by

$$\mathbf{y} = \mathbf{g}s + \mathbf{v} \quad (2)$$

where \mathbf{v} is the terminals' noise vector. In the second time slot, the k th terminal multiplies its received signal with the complex conjugate of the beamforming weight w_k and forwards the resulting signal to the receiver. It follows from Equation (2) that the received signal at O is

$$\begin{aligned} r &= \mathbf{f}^T (\mathbf{w}^* \odot \mathbf{y}) + n = \mathbf{w}^H (\mathbf{f} \odot \mathbf{y}) + n \\ &= \mathbf{w}^H (\mathbf{f} \odot \mathbf{g}s + \mathbf{f} \odot \mathbf{v}) + n \\ &= s\mathbf{w}^H \mathbf{h} + \mathbf{w}^H (\mathbf{f} \odot \mathbf{v}) + n \end{aligned} \quad (3)$$

where $\mathbf{w} \triangleq [w_1, \dots, w_K]$ is the beamforming vector, $\mathbf{h} \triangleq \mathbf{f} \odot \mathbf{g}$, $\mathbf{f} \triangleq [f_1, \dots, f_K]^T$, and n is the receiver noise. As mentioned earlier, several approaches can be adopted to properly select the beamforming weights. In this paper, we are only concerned with the approach that aims to minimize the noise power while fixing the beamforming response in the desired direction equal to 1. Several beamformers based on different channel models exist in the literature to perform these tasks. If \mathbf{w}_\star denotes the beamforming vector associated with one of these beamformers, it is then the solution of the following optimization problem:

$$\mathbf{w}_\star = \arg \min P_{\mathbf{w},n}^r \quad \text{s.t.} \quad \mathbf{w}^H \mathbf{h}_\star = 1 \quad (4)$$

where \mathbf{h}_\star is the considered nominal channel when designing \mathbf{w}_\star and $P_{\mathbf{w},n}^r$ is the aggregate noise power due to the thermal noise at the receiver and the forwarded noises from the terminals given by

$$P_{\mathbf{w},n}^r = \sigma_v^2 \mathbf{w}^H \mathbf{\Lambda} \mathbf{w} + \sigma_n^2 \quad (5)$$

where $\mathbf{\Lambda} \triangleq \text{diag}\{[f]_1|^2, \dots, [f]_K|^2\}$. Using Equation (5) in Equation (4), we obtain the following optimization problem:

$$\mathbf{w}_\star = \arg \min \mathbf{w}^H \mathbf{\Lambda} \mathbf{w} \quad \text{s.t.} \quad \mathbf{w}^H \mathbf{h}_\star = 1 \quad (6)$$

It can be readily proven that \mathbf{w}_\star is given by

$$\mathbf{w}_\star = \mu_\star \mathbf{\Lambda}^{-1} \mathbf{h}_\star \quad (7)$$

where μ_\star is the factor chosen such that the constraint in Equation (6) is satisfied. In the sequel, we will explore the main existing beamforming solutions and compare their performances.

3.1.1. Rx optimal CB.

The Rx OCB is the well-known CSI-based solution, and hence, its beamforming vector is given by [19–23]

$$\mathbf{w}_O = \mu_O \mathbf{\Lambda}^{-1} \mathbf{h}_O \quad (8)$$

where $\mathbf{h}_O = \mathbf{h}$ and $\mu_O = (\mathbf{h}_O^H \mathbf{\Lambda}^{-1} \mathbf{h}_O)^{-1}$. From Equation (8), in order to implement the Rx OCB technique, the source must estimate and quantize the channels $[\mathbf{h}]_k$, $k = 1, \dots, K$, before sending them back to all K terminals. This process unfortunately results in both estimation and quantization errors as well as an important overhead. Let us denote the resulting channel vector by $\hat{\mathbf{h}}_O = \mathbf{h}_O + \mathbf{e}_O$ where $\mathbf{e}_O = \mathbf{f} \odot \mathbf{e}_c + \mathbf{f} \odot \mathbf{e}_{cq}$, and \mathbf{e}_c and \mathbf{e}_{cq} are the channel identification and quantization errors, respectively. Let us denote the variance of \mathbf{e}_O by $\sigma_{\mathbf{e}_O}^2 = \sigma_{\mathbf{e}_c}^2 + \sigma_{\mathbf{e}_{cq}}^2$ where $\sigma_{\mathbf{e}_c}^2$ and $\sigma_{\mathbf{e}_{cq}}^2$ are the variances of \mathbf{e}_c and \mathbf{e}_{cq} , respectively. It can be shown that $\sigma_{\mathbf{e}_c}^2$ is given by [26]

$$\sigma_{\mathbf{e}_c}^2 = \frac{3K}{2} \left(\pi \sigma_v^2 \bar{f}_D \right)^{\frac{2}{3}} \quad (9)$$

where \bar{f}_D is the normalized Doppler frequency and $\sigma_{\mathbf{e}_{cq}}^2$ is assumed to be incurred by $(B_c + 1)$ -bit uniform quantization and, hence, is given by [27]

$$\sigma_{\mathbf{e}_{cq}}^2 = 2^{-2B_c} \frac{h_{\text{Max}}^2}{12} \quad (10)$$

where h_{Max} is the peak amplitude of all channels' realizations $[\mathbf{h}]_k$ for $k = 1, \dots, K$. Taking into account these definitions, the OCB's beamforming vector is now given by

$$\hat{\mathbf{w}}_O = \hat{\mu}_O \mathbf{\Lambda}^{-1} \hat{\mathbf{h}}_O \quad (11)$$

where $\hat{\mu}_O = (\hat{\mathbf{h}}_O^H \mathbf{\Lambda}^{-1} \hat{\mathbf{h}}_O)^{-1}$.

3.1.2. Rx monochromatic DCB.

Alternatively, when designing the Rx CB solution, we intentionally neglect the local scattering effect (i.e., assume that $\sigma_\theta \rightarrow 0$) to nominally assume a monochromatic single-ray propagation channel, and hence, the beamforming vector associated with the Rx M-DCB is given by [13]

$$\mathbf{w}_M = \mu_M \mathbf{\Lambda}^{-1} \mathbf{h}_M \quad (12)$$

where $\mathbf{h}_M = \mathbf{a}(0)$, $[\mathbf{a}(\theta)]_k = [\mathbf{f}]_k e^{-j(2\pi/\lambda)r_k \cos(\theta + \phi_s - \psi_k)}$ and $\mu_M = \left(\mathbf{a}(0)^H \mathbf{\Lambda}^{-1} \mathbf{a}(0) \right)^{-1} = 1/K$. Also known as conventional Rx DCB, this beamformer implementation requires that the source estimates, quantizes, and sends its direction ϕ_s only [1]. This process results in both localization and quantization errors and, hence, the channel \mathbf{h}_M should be substituted by

$$\hat{\mathbf{h}}_M = \mathbf{h}_M e^{-j(\mathbf{e}_a + \mathbf{e}_{aq})} \quad (13)$$

where \mathbf{e}_a and \mathbf{e}_{aq} are the angle localization and quantization errors, respectively. Assuming that these errors are relatively small and using Taylor's series expansion, one can easily prove that

$$\hat{\mathbf{h}}_M \simeq \mathbf{h}_M + \mathbf{e}_M \quad (14)$$

where $\mathbf{e}_M = -j\mathbf{h}_M(\mathbf{e}_a + \mathbf{e}_{aq})$ with variance $\sigma_{\mathbf{e}_M}^2 = \sigma_{\mathbf{e}_a}^2 + \sigma_{\mathbf{e}_{aq}}^2$. Using a $(B_a + 1)$ -bit uniform quantization, it can be shown that [27]

$$\sigma_{\mathbf{e}_{aq}}^2 = 2^{-2B_a} \frac{4\pi^2}{12} \quad (15)$$

Furthermore, we use the Cramér–Rao lower bound (CRLB) developed in [28] to define $\sigma_{\mathbf{e}_a}^2$ as

$$\sigma_{\mathbf{e}_a}^2 = \frac{4 \sin^2\left(\frac{\pi}{K}\right) \sigma_v^2}{NK\pi^2} \quad (16)$$

where N is the number of samples used to estimate ϕ_s . Taking into account the aforementioned definitions, the practical M-DCB beamforming vector is now given by

$$\hat{\mathbf{w}}_M = \hat{\mu}_M \mathbf{\Lambda}^{-1} \hat{\mathbf{h}}_M \quad (17)$$

where $\hat{\mu}_M = \left(\hat{\mathbf{h}}_M^H \mathbf{\Lambda}^{-1} \hat{\mathbf{h}}_M \right)^{-1}$

3.1.3. Rx bichromatic distributed CB.

Exploiting the fact that for low AS, a multi-ray channel—owing to a Taylor series expansion of its correlation matrix—can be properly approximated by two angular rays and hence considered as bichromatic, a B-DCB was recently proposed in [24] and [25]. Its beamforming vector is given by

$$\mathbf{w}_B = \mu_B \mathbf{\Lambda}^{-1} \mathbf{h}_B \quad (18)$$

where

$$\mathbf{h}_B = \frac{1}{2} (\mathbf{a}(\sigma_\theta) + \mathbf{a}(-\sigma_\theta)) \quad (19)$$

and

$$\begin{aligned} \mu_B &= \frac{2}{K} \lim_{K \rightarrow \infty} \left(\frac{\|\mathbf{a}(\sigma_\theta)\|^2}{K} + \text{Re} \left\{ \frac{\mathbf{a}(\sigma_\theta)^H \mathbf{\Lambda}^{-1} \mathbf{a}(-\sigma_\theta)}{K} \right\} \right)^{-1} \\ &= \frac{2}{K} \left(1 + 2 \frac{J_1(\gamma(2\sigma_\theta))}{\gamma(2\sigma_\theta)} \right)^{-1} \end{aligned} \quad (20)$$

where $\gamma(\phi) = (4\pi R/\lambda) \sin(\phi/2)$. Note that in the conventional Rx scenario where the local scattering effect is neglected (i.e., $\sigma_\theta \rightarrow 0$) to assume monochromatic propagation channels, Equation (18) is reduced to Equation (12). It is also noteworthy that the Rx B-DCB's implementation requires that the source estimates, quantizes, and sends its direction ϕ_s and the AS σ_θ , thereby resulting in both estimation and quantization errors. The channel \mathbf{h}_B should be then substituted by

$$\hat{\mathbf{h}}_B = \mathbf{h}_B e^{-j(\mathbf{e}_a + \mathbf{e}_{aq} + \mathbf{e}_s + \mathbf{e}_{sq})} \quad (21)$$

where \mathbf{e}_s and \mathbf{e}_{sq} are the AS estimation and quantization errors, respectively. Using the same approach as mentioned earlier, one can easily show for relatively small errors that

$$\hat{\mathbf{h}}_B = \mathbf{h}_B + \mathbf{e}_B \quad (22)$$

where $\mathbf{e}_B = -j\mathbf{h}_B(\mathbf{e}_a + \mathbf{e}_{aq} + \mathbf{e}_s + \mathbf{e}_{sq})$ with variance $\sigma_{\mathbf{e}_B}^2 = \sigma_{\mathbf{e}_a}^2 + \sigma_{\mathbf{e}_{aq}}^2 + \sigma_{\mathbf{e}_s}^2 + \sigma_{\mathbf{e}_{sq}}^2$. Using a $(B_s + 1)$ -bit uniform quantization, it can be shown that [27]

$$\sigma_{\mathbf{e}_{sq}}^2 = 2^{-2B_s} \frac{\pi^2}{12} \quad (23)$$

Because AS estimation can be modeled as a direction of arrival (DoA) estimation of two point sources, we also use for simplicity the CRLB developed in [28] to define $\sigma_{\mathbf{e}_s}^2$, and hence, $\sigma_{\mathbf{e}_s}^2 = \sigma_{\mathbf{e}_a}^2$. Therefore, the B-DCB beamforming weight is now

$$\hat{\mathbf{w}}_B = \hat{\mu}_B \mathbf{\Lambda}^{-1} \hat{\mathbf{h}}_B \quad (24)$$

where

$$\hat{\mu}_B = \frac{2}{K} \left(1 + \sigma_{\mathbf{e}_B}^2 \right)^{-1} \left(1 + 2 \frac{J_1(\gamma(2\sigma_\theta))}{\gamma(2\sigma_\theta)} \right)^{-1} \quad (25)$$

In the sequel, we will analyze and compare the performances of all the aforementioned Rx CB designs. Before doing so, let us turn our attention to the Tx CB configuration.

3.2. Tx CB configuration

In this scheme (cf. Figure 1(b)), a dual-hop communication is also considered from the source S to the receiver. In the

first time slot, the source sends its signal s to the terminals, whereas in the second time slot, the k th terminal multiplies its received signal with the complex conjugate of the beamforming weight w_k and forwards the resulting signal to the far-field receiver. In order to select w_k for $k = 1, \dots, K$, the same criterion as aforementioned is used, and hence, any beamforming solution with beamforming vector \mathbf{w}_\star^t satisfies

$$\mathbf{w}_\star^t = \arg \min P_{\mathbf{w},n}^t \quad \text{s.t.} \quad \mathbf{w}^H \mathbf{h}_\star = 1 \quad (26)$$

where $P_{\mathbf{w},n}^t$ is the aggregate noise power given by [24]

$$P_{\mathbf{w},n}^t = \sigma_v^2 \mathbf{w}^H \mathbf{w} + \sigma_n^2 \quad (27)$$

It can be easily shown that \mathbf{w}_\star^t is given by

$$\mathbf{w}_\star^t = \mu_\star^t \mathbf{h}_\star \quad (28)$$

where μ_\star^t is chosen such that \mathbf{w}_\star^t satisfies the constraint in Equation (26).

3.2.1. Tx optimal CB.

The Tx OCB is a CSI-based solution, and hence, its beamforming vector is given by

$$\mathbf{w}_O^t = \mu_O^t \mathbf{h}_O \quad (29)$$

where $\mathbf{h}_O = \mathbf{h}$ and $\mu_O^t = 1/\|\mathbf{h}_O\|^2$. Similarly to \mathbf{w}_O , the Tx OCB's implementation requires that the source estimates and quantizes the channels $[\mathbf{h}]_k, k = 1, \dots, K$, before sending them back to all K terminals. This process obviously results in estimation and quantization errors, and hence, the considered channel \mathbf{h}_O must be substituted by $\hat{\mathbf{h}}_O$. Therefore, \mathbf{w}_O^t becomes

$$\hat{\mathbf{w}}_O^t = \hat{\mu}_O^t \hat{\mathbf{h}}_O \quad (30)$$

where $\hat{\mu}_O^t = 1/\|\hat{\mathbf{h}}_O\|^2$.

3.2.2. Tx monochromatic DCB.

If we neglect the local scattering effect (i.e., assume that $\sigma_\theta \rightarrow 0$) to assume monochromatic single-ray propagation channels, the optimal solution of Equation (26) becomes

$$\mathbf{w}_M^t = \mu_M^t \mathbf{h}_M \quad (31)$$

the beamforming vector associated with the Tx M-DCB also known as the conventional Tx DCB [3]. In Equation (31), $\mu_M^t = 1/\|\mathbf{h}_M\|^2$. It is noteworthy that the implementation of this beamformer requires that the source estimates, quantizes, and sends its direction ϕ_s only, thereby resulting in estimation and quantization errors that affect the considered channel \mathbf{h}_M . Substituting \mathbf{h}_M by $\hat{\mathbf{h}}_M$ when designing the Tx M-DCB, we obtain a new beamforming vector

$$\hat{\mathbf{w}}_M^t = \hat{\mu}_M^t \hat{\mathbf{h}}_M \quad (32)$$

where $\hat{\mu}_M^t = 1/\|\hat{\mathbf{h}}_M\|^2$.

3.2.3. Tx bichromatic DCB.

In [24], we also propose a Tx B-DCB whose beamforming vector is

$$\mathbf{w}_B^t = \mu_B \mathbf{h}_B \quad (33)$$

Please note that the implementation of \mathbf{w}_B^t is similar to that of \mathbf{w}_O , and hence, the channel \mathbf{h}_B should be substituted by $\hat{\mathbf{h}}_B$ when designing the Tx B-DCB. Using similar steps as in Section 3.1.3, it can be shown that the beamforming vector associated with the Tx B-DCB is

$$\mathbf{w}_B^t = \hat{\mu}_B \hat{\mathbf{h}}_B \quad (34)$$

4. PERFORMANCE ANALYSIS IN TERMS OF ASANR

For the sake of simplicity, in what follows, we only focus on the Rx CB configuration, but it is straightforward to show that all the results and deductions also hold for the Tx CB configuration. In this section, we analyze and compare the performance of the Rx B-DCB against those of the Rx M-DCB and OCB. To this end, we introduce the following performance measure:

$$\Upsilon_\star(\sigma_\theta) = \frac{\xi_{\hat{\mathbf{w}}_\star}}{\xi_{\hat{\mathbf{w}}_B}} \quad (35)$$

where

$$\xi_{\mathbf{w}} = \frac{P_{\mathbf{w}}(\phi_s)}{P_{\mathbf{w},n}^r} \quad (36)$$

is the achieved SNR when the beamforming vector \mathbf{w} is used. $\Upsilon_\star(\sigma_\theta)$ hence interprets the SNR gain achieved by the beamformer $\hat{\mathbf{w}}_\star$ against the B-DCB design. In Equation (36), commonly known as the beampattern, $P_{\mathbf{w}}(\phi_s) = p_\star \left| \mathbf{w}^H \mathbf{h} \right|^2 = p_\star \left| \mathbf{w}^H \sum_{l=1}^L \alpha_l \mathbf{a}(\phi_s + \theta_l) \right|^2$ is the received power from a transmitter at direction ϕ_s with power p_\star . It is noteworthy that $\Upsilon_\star(\sigma_\theta)$ is an excessively complex function of the random variables r_k, ψ_k , and $[\mathbf{f}]_k$ for $k = 1, \dots, K$, and α_l, θ_l for $l = 1, \dots, L$, as well as all the estimation and quantization errors and, hence, a random quantity of its own. Therefore, it is practically more appealing to investigate the behavior and the properties of $\tilde{\Upsilon}_\star(\sigma_\theta)$ given by [13,25]

$$\tilde{\Upsilon}_\star(\sigma_\theta) = \frac{\tilde{\xi}_{\hat{\mathbf{w}}_\star}}{\tilde{\xi}_{\hat{\mathbf{w}}_B}} \quad (37)$$

where $\tilde{\xi}_{\mathbf{w}} = \tilde{P}_{\mathbf{w}}(\phi_s)/\tilde{P}_{\mathbf{w},n}^r$ is the achieved ASANR when \mathbf{w} is implemented with $\tilde{P}_{\mathbf{w}}(\phi_s) = E\{P_{\mathbf{w}}(\phi_s)\}$, called the average beampattern, and $\tilde{P}_{\mathbf{w},n}^r = E\{P_{\mathbf{w},n}^r\}$ is the average noise power. In ideal conditions where all the estimation and quantization errors are negligible, we define the following performance measure:

$$\tilde{\Upsilon}_\star^{\text{IDL}}(\sigma_\theta) = \frac{\tilde{\xi}_{\hat{\mathbf{w}}_\star}}{\tilde{\xi}_{\hat{\mathbf{w}}_B}} \quad (38)$$

Before comparing the beamformers' performances, we derive the expression of the ASANR $\tilde{\xi}_{\hat{\mathbf{w}}_\star}$ achieved using $\hat{\mathbf{w}}_\star$. First, we have

$$\tilde{\xi}_{\hat{\mathbf{w}}_\star} = \frac{\mu_\star^2 \|(\mathbf{h}_\star^H + \mathbf{e}_\star^H) \mathbf{\Lambda}^{-1} \mathbf{h}\|^2}{\sigma_v^2 \mu_\star^2 (\mathbf{h}_\star^H + \mathbf{e}_\star^H) \mathbf{\Lambda}^{-1} (\mathbf{h}_\star + \mathbf{e}_\star) + \sigma_n^2 \left(\frac{\mu_\star}{\hat{\mu}_\star}\right)^2} \quad (39)$$

Using the fact that \mathbf{h} and \mathbf{e}_\star are statistically independent, $\tilde{\xi}_{\hat{\mathbf{w}}_\star}$ can then be expressed as

$$\begin{aligned} \tilde{\xi}_{\hat{\mathbf{w}}_\star} &= \frac{\mathbb{E}\{\|\mathbf{w}_\star^H \mathbf{h}\|^2\} + \mathbb{E}\left\{\mu_\star^2 \|\mathbf{h}^H \mathbf{\Lambda}^{-1} \mathbf{e}_\star\|^2\right\}}{\sigma_v^2 \mathbb{E}\{\mathbf{w}_\star^H \mathbf{\Lambda} \mathbf{w}_\star\} + \sigma_v^2 \mathbb{E}\left\{\mu_\star^2 \mathbf{e}_\star^H \mathbf{\Lambda}^{-1} \mathbf{e}_\star\right\} + \sigma_n^2 \mathbb{E}\left\{\left(\frac{\mu_\star}{\hat{\mu}_\star}\right)^2\right\}} \\ &= \frac{\tilde{P}_{\mathbf{w}_\star}(\phi_s) + \mathbb{E}\left\{\mu_\star^2 \|\mathbf{h}^H \mathbf{\Lambda}^{-1} \mathbf{e}_\star\|^2\right\}}{\tilde{P}_{\mathbf{w}_\star, n}^r + \sigma_v^2 \mathbb{E}\left\{\mu_\star^2 \mathbf{e}_\star^H \mathbf{\Lambda}^{-1} \mathbf{e}_\star\right\} + \sigma_n^2 \left(\mathbb{E}\left\{\left(\frac{\mu_\star}{\hat{\mu}_\star}\right)^2\right\} - 1\right)} \end{aligned} \quad (40)$$

Note that both numerator and denominator decomposes each into two terms corresponding to a channel mismatch contribution (i.e., $\tilde{P}_{\mathbf{w}_\star}(\phi_s)$ or $\tilde{P}_{\mathbf{w}_\star, n}^r$, respectively) and a channel quantization/estimation errors contribution (i.e., the remainder of each term).

4.1. ASANR of B-DCB versus OCB

In this section, we carry out a comparison between the B-DCB and its OCB vis-a-vis. When the OCB technique is implemented in the network, it can be readily shown that

$$\tilde{P}_{\mathbf{w}_0, n}^r = \sigma_v^2 \mathbb{E}\left\{\frac{1}{\|\mathbf{g}\|^2}\right\} + \sigma_n^2 \quad (41)$$

and

$$\tilde{P}_{\mathbf{w}_0}(\phi_\star) = 1 \quad (42)$$

We can also show that

$$\mathbb{E}\left\{\mu_0^2 \|\mathbf{h}^H \mathbf{\Lambda}^{-1} \mathbf{e}_0\|^2\right\} = \sigma_{\mathbf{e}_0}^2 \mathbb{E}\left\{\frac{1}{\|\mathbf{g}\|^2}\right\} \quad (43)$$

and

$$\sigma_v^2 \mathbb{E}\left\{\mu_0^2 \mathbf{e}_0^H \mathbf{\Lambda}^{-1} \mathbf{e}_0\right\} = K \sigma_{\mathbf{e}_0}^2 \sigma_v^2 \mathbb{E}\left\{\frac{1}{\|\mathbf{g}\|^4}\right\} \quad (44)$$

Now, let us introduce the following theorem:

Theorem 1. Assuming that α_l for $l = 1, \dots, L$, are Gaussian random variables, we have

$$\begin{aligned} \mathbb{E}\left\{\frac{1}{\|\mathbf{g}\|^2}\right\} &= \frac{1}{K} \mathbb{E}\left\{\frac{1}{\sum_{l=1}^L |\alpha_l|^2}\right\} \\ &= \frac{L}{K(L-1)} \end{aligned} \quad (45)$$

and

$$\begin{aligned} \mathbb{E}\left\{\frac{1}{\|\mathbf{g}\|^4}\right\} &= \frac{1}{K^2} \mathbb{E}\left\{\frac{1}{\left(\sum_{l=1}^L |\alpha_l|^2\right)^2}\right\} \\ &= \frac{L^2}{K^2(L-1)(L-2)} \end{aligned} \quad (46)$$

Proof. See Appendix A. \square

In order to derive a closed-form expression for $\tilde{\gamma}_0$, we need to derive $\mathbb{E}\left\{(\mu_0/\hat{\mu}_0)^2\right\}$. However, the latter turns out to be intractable in closed-form, and this unfortunately hampers a rigorous analytical study of $\tilde{\gamma}_0$. Nevertheless, when K is large enough, we show that[†]

$$\begin{aligned} \tilde{\xi}_{\hat{\mathbf{w}}_0} &= \left(\sigma_n^2 \mathbb{E}\left\{\lim_{K \rightarrow \infty} \left(\frac{\mu_0}{\hat{\mu}_0}\right)^2\right\}\right)^{-1} \\ &= \left(\sigma_n^2 \left(1 + 2 \frac{\sigma_{\mathbf{e}_0}^2 L}{L-1} + \frac{\sigma_{\mathbf{e}_0}^4 L^2}{(L-1)(L-2)}\right)\right)^{-1} \end{aligned} \quad (47)$$

Therefore, it follows from Equations (9), (10), and (47) that the ASANR achieved by the OCB technique decreases when the normalized Doppler spread \tilde{f}_D increases while it increases if B_c increases. However, we will see in Section 5.1 that we cannot indefinitely increase B_c because this has a detrimental effect on the achieved throughput.

In turn, using the B-DCB technique, we have [24,25]

$$\tilde{P}_{\mathbf{w}_B, n}^r = \frac{2\sigma_v^2}{K} \left(1 + 2 \frac{J_1(\gamma(2\sigma_\theta))}{\gamma(2\sigma_\theta)}\right)^{-1} + \sigma_n^2 \quad (48)$$

and

$$\tilde{P}_{\mathbf{w}_B}(\phi_\star) = \frac{2}{K \left(1 + 2 \frac{J_1(\gamma(2\sigma_\theta))}{\gamma(2\sigma_\theta)}\right)} \left(1 + \frac{2(K-1)\Omega(\phi_\star)}{\left(1 + 2 \frac{J_1(\gamma(2\sigma_\theta))}{\gamma(2\sigma_\theta)}\right)}\right) \quad (49)$$

with

$$\begin{aligned} \Omega(\phi) &= \int p(\theta) \left(\frac{J_1(\gamma(\phi + \theta + \sigma_\theta))}{\gamma(\phi + \theta + \sigma_\theta)}\right. \\ &\quad \left. + \frac{J_1(\gamma(\phi + \theta - \sigma_\theta))}{\gamma(\phi + \theta - \sigma_\theta)}\right)^2 d\theta \end{aligned} \quad (50)$$

Note that the integral in Equation (50) can be computed numerically with any desired accuracy by using the most popular mathematical software packages such as MATLAB (MathWorks, Natick, MA, USA) and MATHEMATICA (Wolfram Research, Champaign, IL, USA), after properly choosing the probability density function

[†] Please note that L is in essence an artifact due to channel modeling by a limited number of rays. In practice, L tends to infinity, and all terms in L asymptotically disappear.

$p(\theta)$. In fact, several statistical distributions for θ_l have been proposed so far such as the Laplace, Gaussian, or Uniform distribution [15–18], but here, we are only concerned by the latter. Furthermore, we show that

$$E \left\{ \mu_B^2 \left\| \mathbf{h}^H \mathbf{\Lambda}^{-1} \mathbf{e}_B \right\|^2 \right\} = 2 \frac{\sigma_{e_B}^2}{K} \left(1 + 2 \frac{J_1(\gamma(2\sigma_\theta))}{\gamma(2\sigma_\theta)} \right)^{-1} \quad (51)$$

and

$$E \left\{ \mu_B^2 \mathbf{e}_B^H \mathbf{\Lambda}^{-1} \mathbf{e}_B \right\} = \frac{2\sigma_{e_B}^2}{K} \left(1 + 2 \frac{J_1(\gamma(2\sigma_\theta))}{\gamma(2\sigma_\theta)} \right)^{-1} \quad (52)$$

Therefore, using Equations (25) and (20) as well as Equations (48)–(52), for large K , we obtain

$$\tilde{\xi}_{\hat{\mathbf{w}}_B} = \frac{4\Omega(0) \left(1 + 2 \frac{J_1(\gamma(2\sigma_\theta))}{\gamma(2\sigma_\theta)} \right)^{-2}}{\sigma_n^2 (1 + \sigma_{e_B}^2)^2} \quad (53)$$

It follows from Equation (53) that in contrast with the OCB, which is a CSI-based beamforming solution, the achieved ASANR using B-DCB remains constant when \tilde{f}_D increases. Furthermore, it follows also that increasing B_a and/or B_s results in improving the ASANR achieved using B-DCB. Using Equations (47) and (53), we obtain

$$\tilde{\Upsilon}_O(\sigma_\theta) = \tilde{\Upsilon}_O^{\text{IDL}}(\sigma_\theta) \frac{(1 + \sigma_{e_B}^2)^2}{1 + 2 \frac{\sigma_{e_O}^2 L}{L-1} + \frac{\sigma_{e_O}^4 L^2}{(L-1)(L-2)}} \quad (54)$$

where

$$\tilde{\Upsilon}_O^{\text{IDL}}(\sigma_\theta) = \frac{\left(1 + 2 \frac{J_1(\gamma(2\sigma_\theta))}{\gamma(2\sigma_\theta)} \right)^2}{4\Omega(0)} \quad (55)$$

Given the fact that when \tilde{f}_D increases $\sigma_{e_O}^2$ increases, it can be inferred from Equation (54) that $\tilde{\Upsilon}_O(\sigma_\theta)$ decreases as expected. Moreover, it can be readily proven that $\tilde{\Upsilon}_O^{\text{IDL}}(0) = 1$. This is expected because, when there is no local scattering in the source vicinity (i.e., $\sigma_\theta = 0$), $\mathbf{w}_O = \mathbf{w}_B$. Simulations results in Section 6 will also show that, in rural and suburban areas where σ_θ is small, $\tilde{\Upsilon}_O^{\text{IDL}}(\sigma_\theta) = 1$. Therefore, from Equations (9) and (54), $\tilde{\Upsilon}_O(\sigma_\theta) < 1$ for large \tilde{f}_D and small AS. Consequently, the B-DCB is able to outperform its OCB vis-a-vis when σ_θ is small such as in rural and suburban areas. However, when σ_θ is relatively large such as in urban areas, one can easily show that $J_1(\gamma(2\sigma_\theta))/\gamma(2\sigma_\theta) \simeq 0$ [4], and hence, it holds for large K that $\tilde{\Upsilon}_O^{\text{IDL}}(\sigma_\theta) \simeq (4\Omega(0))^{-1}$. Because $\Omega(0)$ decreases if σ_θ increases, $\tilde{\Upsilon}_O(\sigma_\theta)$ turns out to be a decreasing function of σ_θ for high AS. Consequently, in ideal conditions, the OCB outperforms the B-DCB in terms of ASANR at high AS. However, it follows from Equation (54) that this ASANR gain decreases if \tilde{f}_D increases. Simulations in Section 6 will show that this results in a wider operational region in terms of AS values over which the B-DCB is favored against OCB.

4.2. ASANR of B-DCB versus M-DCB

Using the M-DCB technique, it can be shown that [24,25]

$$\tilde{P}_{\mathbf{w}_M, n}^r = \frac{\sigma_v^2}{K} + \sigma_n^2 \quad (56)$$

and

$$\tilde{P}_{\mathbf{w}_M}(\phi_\star) = \frac{(1 + (K-1)\Gamma(\phi_\star))}{K} \quad (57)$$

with

$$\Gamma(\phi) = \int p(\theta) \left(2 \frac{J_1(\gamma(\phi + \theta))}{\gamma(\phi + \theta)} \right)^2 d\theta \quad (58)$$

Note that the discussion involving the integral in Equation (50) also holds for the integral in Equation (58). Moreover, using similar steps as aforementioned, we show for large K that

$$\tilde{\xi}_{\hat{\mathbf{w}}_B} = \frac{\Gamma(0)}{\sigma_n^2 (1 + \sigma_{e_M}^2)^2} \quad (59)$$

and, hence,

$$\tilde{\Upsilon}_M(\sigma_\theta) = \tilde{\Upsilon}_M^{\text{IDL}}(\sigma_\theta) \left(\frac{1 + \sigma_{e_B}^2}{1 + \sigma_{e_M}^2} \right)^2 \quad (60)$$

where

$$\tilde{\Upsilon}_M^{\text{IDL}}(\sigma_\theta) = \frac{\Gamma(0) \left(1 + 2 \frac{J_1(\gamma(2\sigma_\theta))}{\gamma(2\sigma_\theta)} \right)^2}{4\Omega(0)} \quad (61)$$

In [25], we proved that $\tilde{\Upsilon}_M^{\text{IDL}}(\sigma_\theta) \leq 1$ and the ASANR gain achieved using \mathbf{w}_B instead of \mathbf{w}_M can reach as much as 3 dB for high AS. However, from Equation (60), $\tilde{\Upsilon}_M(\sigma_\theta) < \tilde{\Upsilon}_M^{\text{IDL}}(\sigma_\theta)$ only when $\sigma_{e_B}^2 > \sigma_{e_M}^2$ (i.e., small B_a and B_s). Therefore, the B-DCB always outperforms the M-DCB as found in ideal conditions, excluding exceptional circumstances of unrealistic low quantization levels (i.e., very large quantization errors) that are hard to justify in practice.

5. PERFORMANCE ANALYSIS IN TERMS OF LINK-LEVEL THROUGHPUT

The problem with the comparisons made earlier at the ASANR level is that they do not factor in the different overhead costs incurred by each solution. It is therefore appropriate to make comparisons in terms of the link-level throughput as well. Let $\mathcal{T}_{\hat{\mathbf{w}}_\star}(\sigma_\theta)$ denote the link-level throughput achieved by any beamformer $\hat{\mathbf{w}}_\star$ as follows [29]:

$$\mathcal{T}_{\hat{\mathbf{w}}_\star}(\sigma_\theta) = \frac{1}{2} E \left\{ \left(W - W_{\hat{\mathbf{w}}_\star}^{\text{oh}} \right) \log_2 (1 + \xi_{\hat{\mathbf{w}}_\star}) \right\} \quad (62)$$

where W is the channel bandwidth, $W_{\hat{\mathbf{w}}_*}^{\text{oh}}$ is the bandwidth allocated to the implementation overhead of $\hat{\mathbf{w}}_*$, and the expectation is taken with respect to the random variables r_k , ψ_k , and $[\mathbf{f}]_k$ for $k = 1, \dots, K$, α_l and θ_l for $l = 1, \dots, L$, as well as any estimation and quantization errors. Obviously, $\tilde{\mathcal{T}}_{\hat{\mathbf{w}}_*}(\sigma_\theta)$ is intractable in closed-form, which hampers its analytical study. However, knowing that $\log_2(x)$ is a concave function and using Jensen's inequality, we introduce the following upper bound:

$$\mathcal{T}_{\hat{\mathbf{w}}_*}^{\text{bound}}(\sigma_\theta) = \frac{1}{2} \left(W - W_{\hat{\mathbf{w}}_*}^{\text{oh}} \right) \log_2 \left(1 + \mathbb{E} \{ \xi_{\hat{\mathbf{w}}_*} \} \right) \quad (63)$$

where it can be shown that when K is large enough for $\hat{\mathbf{w}}_* \in \{\hat{\mathbf{w}}_O, \hat{\mathbf{w}}_B, \hat{\mathbf{w}}_M\}$, we have [24,25]

$$\mathcal{T}_{\hat{\mathbf{w}}_*}^{\text{bound}}(\sigma_\theta) \xrightarrow{p1} \tilde{\mathcal{T}}_{\hat{\mathbf{w}}_*}(\sigma_\theta) \quad (64)$$

where

$$\tilde{\mathcal{T}}_{\hat{\mathbf{w}}_*}(\sigma_\theta) = \frac{1}{2} \left(W - W_{\hat{\mathbf{w}}_*}^{\text{oh}} \right) \log_2 \left(1 + \tilde{\xi}_{\hat{\mathbf{w}}_*} \right) \quad (65)$$

Without loss of generality, we assume for simplicity a BPSK-modulated transmission, and hence, $\tilde{\mathcal{T}}_{\hat{\mathbf{w}}_*}(\sigma_\theta)$ can be rewritten as

$$\tilde{\mathcal{T}}_{\hat{\mathbf{w}}_*}(\sigma_\theta) = 0.5 \left(R_T - R_{\hat{\mathbf{w}}_*}^{\text{oh}} \right) \log_2 \left(1 + \tilde{\xi}_{\hat{\mathbf{w}}_*} \right) \quad (66)$$

where R_T and $R_{\hat{\mathbf{w}}_*}^{\text{oh}}$ are the transmission bit rate and the overhead bit rate, respectively. Because the tightness of Jensen's inequality has already been proved in [30], the throughput gain given by

$$\mathcal{G}_*(\sigma_\theta) = \frac{\tilde{\mathcal{T}}_{\hat{\mathbf{w}}_*}(\sigma_\theta) - \tilde{\mathcal{T}}_{\hat{\mathbf{w}}_B}(\sigma_\theta)}{\tilde{\mathcal{T}}_{\hat{\mathbf{w}}_B}(\sigma_\theta)} \quad (67)$$

can be used to compare the CBs' performances. Yet, we will shortly see later, both by analysis and simulations, that this simplifying assumption is still able to provide an analytical framework that is extremely insightful qualitatively.

5.1. Throughput of B-DCB versus OCB

As discussed in Section 3.1.1, OCB's implementation requires that the source broadcast all $[\mathbf{h}]_k$, $k = 1, \dots, K$, for all K terminals. This process requires K time slots of B_c bits transmitted at an identification refreshment rate $f_{\text{IR}} = 1/T_{\text{IR}}$ where T_{IR} denotes the refreshment period. It is noteworthy that T_{IR} should satisfy $T_{\text{IR}} \geq T_c$ where $T_c = 0.423/f_D$ is the coherence time and f_D is the maximum Doppler frequency. For simplicity, we assume $f_{\text{IR}} = 2f_D$. Therefore, the OCB implementation overhead rate is $R_{\hat{\mathbf{w}}_O}^{\text{oh}} = 2KB_c f_D$, and hence, its achieved throughput is

$$\tilde{\mathcal{T}}_{\hat{\mathbf{w}}_O}(\sigma_\theta) = 0.5R_T \left(1 - 2KB_c \bar{f}_D \right) \log_2 \left(1 + \tilde{\xi}_{\hat{\mathbf{w}}_O} \right) \quad (68)$$

As can be observed from Equation (68), the achieved throughput using the OCB technique decreases if the number of terminals K increases. Furthermore, because when \bar{f}_D increases, \mathbf{e}_c increases and $\tilde{\xi}_{\hat{\mathbf{w}}_O}$ decreases, it follows then from the aforementioned result that $\tilde{\mathcal{T}}_{\hat{\mathbf{w}}_O}$ also decreases if \bar{f}_D increases. Interestingly, from Equation (68), B_c has two contradictory effects on $\tilde{\mathcal{T}}_{\hat{\mathbf{w}}_O}$. Indeed, if B_c increases the OCB overhead rate increases, and hence, $\tilde{\mathcal{T}}_{\hat{\mathbf{w}}_O}$ is decreased. However, as discussed earlier, increasing B_c improves the ASANR $\tilde{\xi}_{\hat{\mathbf{w}}_O}$, and therefore, the achieved throughput $\tilde{\mathcal{T}}_{\hat{\mathbf{w}}_O}$ is increased. The result in Equation (68) could then be exploited to find the optimum number of quantization bits B_c^{opt} that maximizes the throughput achieved using the OCB technique.

On the other hand, the B-DCB implementation requires that the source estimates, quantizes, and broadcasts ϕ_s and σ_θ . Broadcasting the angular estimate requires only one time slot of B_a bits transmitted at a localization refreshment rate $f_{\text{LR}} = 1/T_{\text{LR}}$ where T_{LR} is the refreshment period. In turn, broadcasting the AS estimate requires one time slot of B_s bits transmitted at an estimation refreshment rate $f_{\text{ER}} = 1/T_{\text{ER}}$ where T_{ER} is the estimation refreshment period. Consequently, the B-DCB implementation overhead is

$$R_{\hat{\mathbf{w}}_B}^{\text{oh}} = B_a f_{\text{LR}} + B_s f_{\text{ER}} \quad (69)$$

Because T_{LR} and T_{ER} are typically very large compared with T_{IR} (i.e., $T_{\text{LR}} \gg T_{\text{IR}}$ and $T_{\text{ER}} \gg T_{\text{IR}}$), we have both f_{LR} and f_{ER} negligible compared with f_{IR} (i.e., $f_{\text{LR}} \simeq 0$ and $f_{\text{ER}} \simeq 0$), and hence, we have $R_{\hat{\mathbf{w}}_B}^{\text{oh}} \simeq 0$. Therefore, the throughput achieved using the B-DCB is

$$\tilde{\mathcal{T}}_{\hat{\mathbf{w}}_B}(\sigma_\theta) \simeq 0.5R_T \log_2 \left(1 + \tilde{\xi}_{\hat{\mathbf{w}}_B} \right) \quad (70)$$

As can be shown from Equation (70), in contrast to OCB, the B-DCB throughput is independent of the number of terminals K and the normalized Doppler frequency \bar{f}_D , and therefore, $\mathcal{G}_O(\sigma_\theta)$ decreases if K and/or \bar{f}_D increases. Furthermore, because we showed in Section 4.1 that $\tilde{\xi}_{\hat{\mathbf{w}}_B} \geq \tilde{\xi}_{\hat{\mathbf{w}}_O}$ for high SNR and relatively large B_a and B_s , we have

$$\mathcal{G}_O(\sigma_\theta) < 0 \quad (71)$$

for large K and low AS. Consequently, the B-DCB outperforms, in rural and suburban areas, its OCB vis-a-vis in terms of achieved throughput. Simulations in Section 6 will show that this results in a wider operational region in terms of AS values over which the B-DCB is favored against OCB. They will also establish that this operational region increases with K and \bar{f}_D and reaches as much as 40° for large K and high \bar{f}_D , against about 17° in ideal conditions (i.e., without accounting for any overhead cost or any quantization or estimation error). This further proves the efficiency the B-DCB technique.

5.2. Throughput of B-DCB versus M-DCB

As discussed in Section 3.1.2, the M-DCB implementation only requires that the source estimates, quantizes, and broadcasts its angle ϕ_s . Following similar steps as aforementioned, it can be easily shown that $R_{\hat{\mathbf{w}}_M}^{\text{oh}} \simeq 0$, and therefore,

$$\tilde{\Upsilon}_{\hat{\mathbf{w}}_M}(\sigma_\theta) \simeq 0.5R_T \log_2 \left(1 + \tilde{\xi}_{\hat{\mathbf{w}}_M} \right) \quad (72)$$

Thus, from Equations (70) and (72), we obtain

$$\mathcal{G}_M(\sigma_\theta) \simeq \frac{\log_2 \left(1 + \tilde{\xi}_{\hat{\mathbf{w}}_M} \right)}{\log_2 \left(1 + \tilde{\xi}_{\hat{\mathbf{w}}_B} \right)} - 1 \quad (73)$$

Because $\tilde{\xi}_{\hat{\mathbf{w}}_M} \leq \tilde{\xi}_{\hat{\mathbf{w}}_B}$ for reasonable B_s and B_a , we have $\mathcal{G}_M(\sigma_\theta) \leq 0$. It follows from Equation (73) that the B-DCB is always more efficient than the M-DCB in terms of achieved throughput.

6. SIMULATION RESULTS

Numerical experiments are performed to verify the analytical results. In all examples, we assume that the noises' powers σ_n^2 and σ_v^2 are 10 dB below the source transmit power p_s and $K = 20$ (except for Figure 8 in which K varies). It is also assumed that ϕ_s and σ_θ are estimated using $N = 10$ samples. Furthermore, we assume that the number of rays is $L = 6$ and that their phases are uniformly distributed. All the results are obtained by averaging over 10^6 random realizations of $r_k, \psi_k, [\mathbf{f}]_k$ for $k = 1, \dots, K$, and α_l, θ_l for $l = 1, \dots, L$, as well as all the estimation and quantization errors. For the sake of conciseness, we only report and discuss the simulation results obtained in the Rx CB configuration because those obtained in the Tx CB configuration are quite similar.

Figure 2 displays $\tilde{\Upsilon}_M^{\text{IDL}}(\sigma_\theta)$ and $\tilde{\Upsilon}_M(\sigma_\theta)$ for different values of $B = B_a = B_s$. From this figure, we confirm that analytical results match perfectly their empirical counterparts. As can be observed from Figure 2, for a practical value $B = 8$, $\tilde{\Upsilon}_M(\sigma_\theta) \simeq \tilde{\Upsilon}_M^{\text{IDL}}(\sigma_\theta)$. This is expected because for high quantization levels, quantization errors are negligible. In such a case, we also show that the B-DCB is much more efficient in terms of achieved ASANR than its M-DCB vis-a-vis. However, from Figure 2, the achieved ASANR gain using $\hat{\mathbf{w}}_B$ instead of $\hat{\mathbf{w}}_M$ decreases with B . This is expected because $\tilde{\xi}_{\hat{\mathbf{w}}_B}$ is affected by both quantization errors \mathbf{e}_{aq} and \mathbf{e}_{sq} , whereas $\tilde{\xi}_{\hat{\mathbf{w}}_M}$ involves only \mathbf{e}_{aq} . Furthermore, it follows from this figure that the M-DCB outperforms the B-DCB only for unrealistic low quantization levels, which are hard to justify in practice. This corroborates the discussion made in Section 4.2.

Figure 3 shows $\tilde{\Upsilon}_O^{\text{IDL}}(\sigma_\theta)$ and $\tilde{\Upsilon}_O(\sigma_\theta)$ for $\tilde{f}_D = 0$ and different values of $B = B_a = B_s = B_c$. From this figure we confirm that analytical results match perfectly their empirical counterparts. As can be seen from Figure 3,

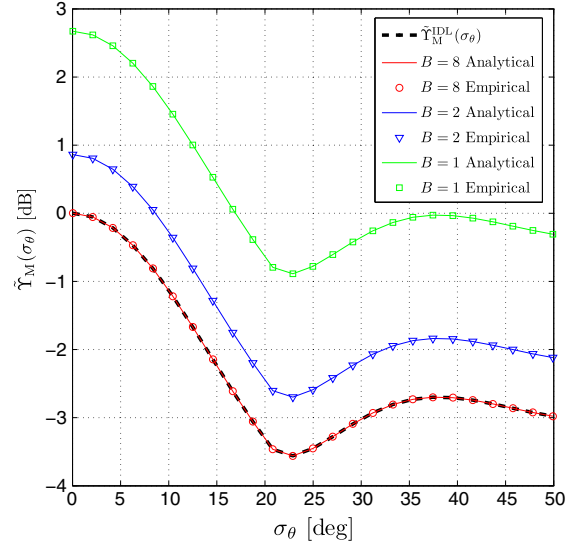


Figure 2. $\tilde{\Upsilon}_M^{\text{IDL}}(\sigma_\theta)$ and $\tilde{\Upsilon}_M(\sigma_\theta)$ for $K = 20$ and different values of $B = B_a = B_s$.

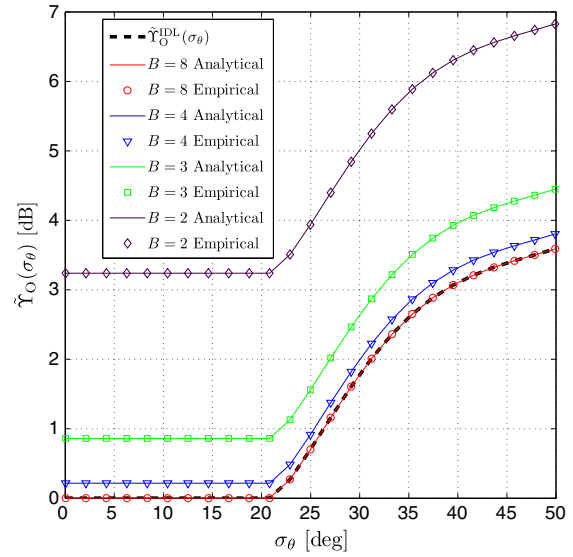


Figure 3. $\tilde{\Upsilon}_O^{\text{IDL}}(\sigma_\theta)$ and $\tilde{\Upsilon}_O(\sigma_\theta)$ for $K = 20$, $\tilde{f}_D = 0$, and different values of $B = B_a = B_s = B_c$.

when $B = 8$, $\tilde{\Upsilon}_O(\sigma_\theta) \simeq \tilde{\Upsilon}_O^{\text{IDL}}(\sigma_\theta)$ as expected. In such a case, the B-DCB is able to achieve the same ASANR as its OCB vis-a-vis when the AS σ_θ is small such as in rural or suburban areas. We also show from Figure 3 that the achieved ASANR gain using $\hat{\mathbf{w}}_O$ instead of $\hat{\mathbf{w}}_B$ increases if B increases. This is expected since in contrast to $\tilde{\xi}_{\hat{\mathbf{w}}_B}$, which involves two quantization errors, $\tilde{\xi}_{\hat{\mathbf{w}}_O}$ involves only \mathbf{e}_{cq} .

Figure 4 plots $\tilde{\Upsilon}_O(\sigma_\theta)$ for $B = B_a = B_s = B_c = 8$ and different values of \tilde{f}_D . From this figure, for low AS, the B-DCB always outperforms the OCB solution even for

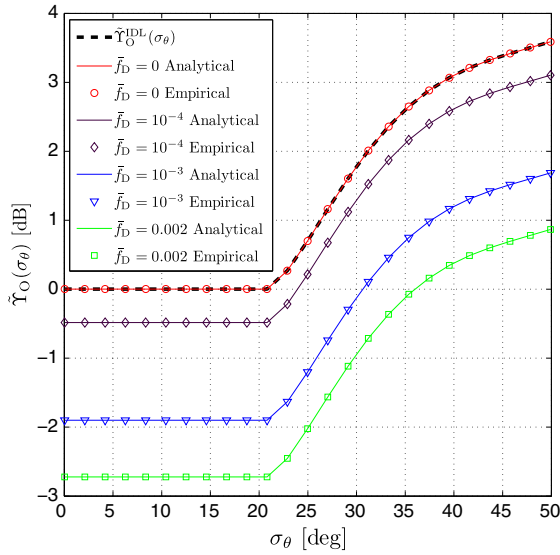


Figure 4. $\tilde{\Upsilon}_O^{\text{IDL}}(\sigma_\theta)$ and $\tilde{\Upsilon}_O(\sigma_\theta)$ for $K = 20$, $B = B_a = B_s = B_c = 8$ bits and different values of \bar{f}_D .

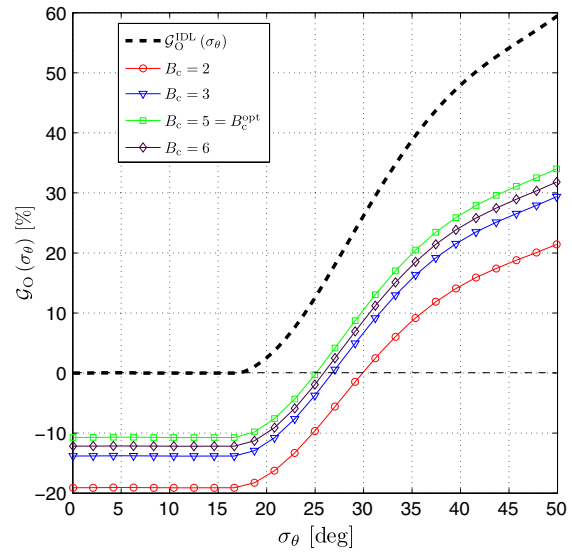


Figure 6. $\mathcal{G}_O(\sigma_\theta)$ for $\bar{f}_D = 10^{-2}$, $K = 20$, and different values of B_c .

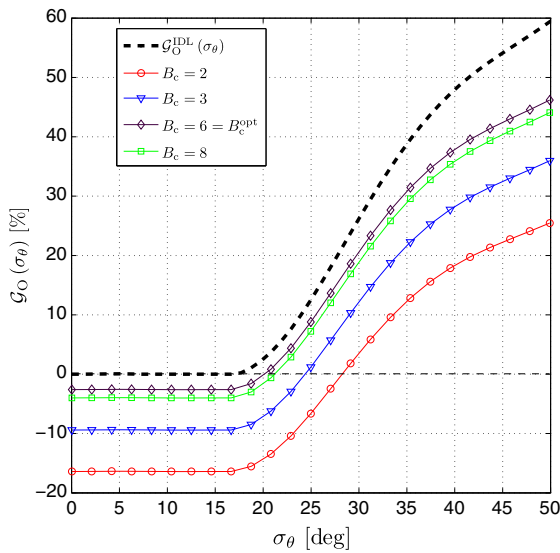


Figure 5. $\mathcal{G}_O(\sigma_\theta)$ for $\bar{f}_D = 10^{-4}$, $K = 20$, and different values of B_c .

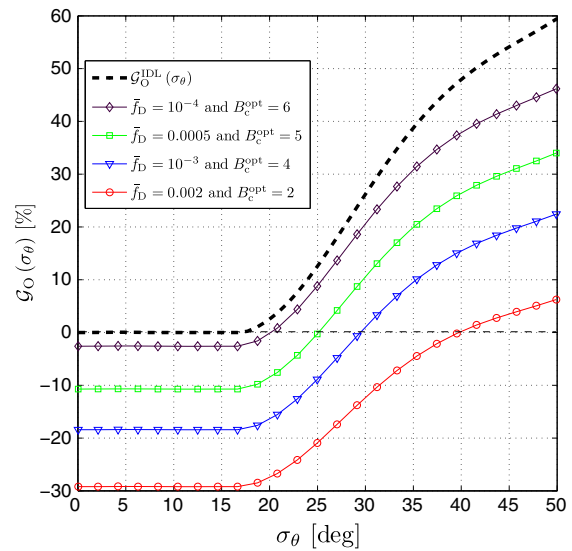


Figure 7. $\mathcal{G}_O(\sigma_\theta)$ for $K = 20$ and different values of \bar{f}_D .

small \bar{f}_D . Furthermore, Figure 4 establishes that the achieved ASANR gain using $\hat{\mathbf{w}}_O$ instead of $\hat{\mathbf{w}}_B$ decreases when \bar{f}_D increases. This corroborates the discussion made in Section 4.1.

Figures 5 and 6 plot the throughput gain $\mathcal{G}_O(\sigma_\theta)$ for different values of \bar{f}_D and B_c . They also plot $\mathcal{G}_O^{\text{IDL}}(\sigma_\theta)$ the throughput gain in ideal conditions (i.e., without accounting for any overhead cost or any quantization or estimation error). As can be observed from these figures, in rural and suburban areas where the AS is relatively low, the B-DCB always outperforms the OCB in terms of achieved throughput. Their performances become actually equal

only in idealistic conditions that ignore the practical effects of both overhead and estimation and quantization errors. Figures 5 and 6 also confirm and illustrate the existence of an optimum quantization level B_c^{opt} that maximizes the throughput (i.e., level that best minimizes combined losses due to errors and overhead) found to be equal to 6 and 5 at \bar{f}_D set to 10^{-4} and 10^{-2} , respectively. At these optimum quantization levels, OCB suffers from throughput losses against B-DCB of about 3% and 10%, respectively. The B-DCB's throughput gains against OCB indeed increase with higher normalized Doppler frequencies. The operational region in terms of AS values over which the B-DCB

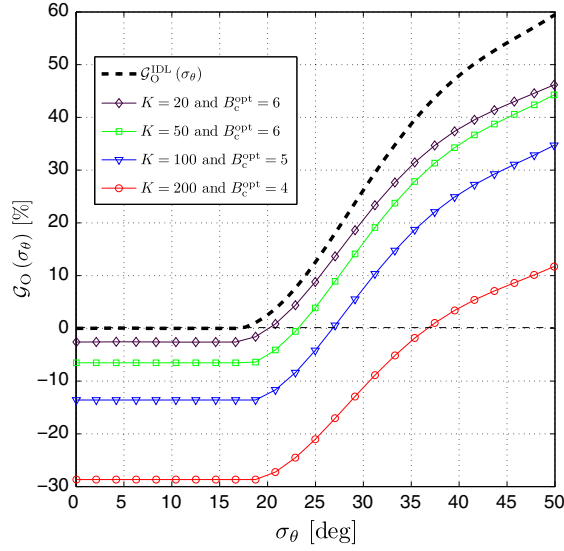


Figure 8. $\mathcal{G}_O(\sigma_\theta)$ for $\bar{f}_D = 10^{-4}$ and different values of K .

is favored against OCB also increases from a nominal low AS range of about 17° in ideal conditions to about 20° and 25° , respectively.

Figures 7 and 8 plot $\mathcal{G}_O(\sigma_\theta)$ for different values of \bar{f}_D and K , respectively. In these figures, curves are plotted after performing a numerical evaluation of the optimum quantization level B_c^{opt} for each pair value of both \bar{f}_D and K . For instance, we find that $B_c^{\text{opt}} = 2$ bits when $\bar{f}_D = 0.002$ and $K = 20$, whereas $B_c^{\text{opt}} = 4$ bits when $\bar{f}_D = 10^{-4}$ and $K = 200$. As can be seen from these figures, the B-DCB's throughput gain against OCB increases if \bar{f}_D and/or K increase(s). Furthermore, the B-DCB operational region also increases if \bar{f}_D and/or K increase(s) and can reach as much as 40° when $\bar{f}_D = 0.002$ and $K = 20$. All these observations corroborate all the elements of our discussion in Section 5.1.

7. CONCLUSION

In this work, we considered the M-DCB and the B-DCB as well as the optimal CSI-based CB (OCB) solution to achieve a dual-hop communication from a source to a receiver through a wireless network comprised of K independent terminals. Assuming the presence of local scattering in the source vicinity and accounting for estimation and quantization errors incurred by each CB solution, we performed an ASANR comparison between all CB solutions and derived their true achieved ASANR in closed-form. For low AS, where both solutions nominally achieve the same ASANR in ideal conditions, we showed that the B-DCB always outperforms OCB, more so at larger regions of AS values when errors increase. Excluding exceptional circumstances of unrealistic low quantization levels (i.e., very large quantization errors) that are hard to justify in practice, we also showed that the new B-DCB

always outperforms the M-DCB as recently found nominally in ideal conditions. This work is also the first to push the performance analysis of CB to the throughput level by taking into account the feedback overhead cost incurred by each solution. We proved both by concordant analysis and simulations that the B-DCB is able to outperform, even for high AS values, the OCB, which is penalized by its prohibitive implementation overhead, especially for a large number of terminals K and/or high Doppler \bar{f}_D . Indeed, it was shown that the operational regions in terms of AS values over which the new B-DCB is favored against OCB in terms of achieved throughput can reach up to 40° .

APPENDIX A: PROOF OF THEOREM 1

From Equation (1), we have

$$\begin{aligned} \|\mathbf{g}\|^2 &= \sum_{k=1}^K \sum_{l=1}^L \alpha_l e^{-j \frac{2\pi r_k}{\lambda} \cos(\theta_l - \psi_k)} \sum_{m=1}^L \alpha_m^* e^{-j \frac{2\pi r_k}{\lambda} \cos(\theta_m - \psi_k)} \\ &= \frac{K}{2L} \sum_{l=1}^L |\sqrt{2L}\alpha_l|^2 \end{aligned} \quad (\text{A.1})$$

Let us introduce $X = \sum_{l=1}^L |\sqrt{2L}\alpha_l|^2$. Assuming that α_l for $l = 1, \dots, L$, are circular complex Gaussian random variables, X could be considered to have a Chi-squared distribution with $2L$ degrees of freedom. Hence, $1/\|\mathbf{g}\|^2 = (2L/K)(1/X)$ where $1/X$ has an inverse Chi-squared distribution with $2L$ degrees of freedom. Therefore, its average is given by

$$\begin{aligned} \mathbb{E} \left\{ \frac{1}{\|\mathbf{g}\|^2} \right\} &= \frac{2L}{K} \mathbb{E} \left\{ \frac{1}{X} \right\} \\ &= \frac{L}{K(L-1)} \end{aligned} \quad (\text{A.2})$$

On the other hand, its second-order moment is given by

$$\begin{aligned} \mathbb{E} \left\{ \frac{1}{\|\mathbf{g}\|^4} \right\} &= \frac{4L^2}{K^2} \mathbb{E} \left\{ \frac{1}{X^2} \right\} \\ &= \frac{4L^2}{K^2} \left(\frac{2}{(2L-2)^2(2L-4)} + \frac{1}{(2L-2)^2} \right) \\ &= \frac{L^2}{K^2(L-1)(L-2)} \end{aligned} \quad (\text{A.3})$$

□

ACKNOWLEDGEMENTS

Work supported by a Canada Research Chair in Wireless Communications and the Discovery Grants Program of NSERC.

REFERENCES

1. Godara LC. Application of antenna arrays to mobile communications, Part II: Beam-forming and direction-of-arrival considerations. *Proceedings of the IEEE* 1997; **85**: 1195–1245.
2. Havary-Nassab V, Shahbazpanahi S, Grami A, Luo Z-Q. Distributed beamforming for relay networks based on second-order statistics of the channel state information. *IEEE Transactions on Signal Processing* 2008; **56**: 4306–4316.
3. Mudumbai R, Brown DR, Madhow U, Poor HV. Distributed transmit beamforming: challenges and recent progress. *IEEE Communications Magazine* 2009; **47**: 102–110.
4. Ochiai H, Mitran P, Poor HV, Tarokh V. Collaborative beamforming for distributed wireless ad hoc sensor networks. *IEEE Transactions on Signal Processing* 2005; **53**: 4110–4124.
5. Zarifi K, Ghraryeb A, Affes S. Distributed beamforming for wireless sensor networks with improved graph connectivity and energy efficiency. *IEEE Transactions on Signal Processing* 2010; **58**: 1904–1921.
6. Pun M, Brown III DR, Poor HV. Opportunistic collaborative beamforming with one-bit feedback. *IEEE Transactions on Wireless Communications* 2009; **8**: 2629–2641.
7. Barriac G, Mudumbai R, Madhow U. Distributed beamforming for information transfer in sensor networks, In *Proceedings of the 3rd International Workshop Information Processing and Sensor Networks*, Berkeley, CA, USA, April 26-27, 2004; 81–88.
8. Mudumbai R, Barriac G, Madhow U. On the feasibility of distributed beamforming in wireless networks. *IEEE Transactions on Wireless Communications* 2007; **6**: 1754–1763.
9. Brown III DR, Prince G, McNeill J. A method for carrier frequency and phase synchronization of two autonomous cooperative transmitters, In *Proceedings of the 5th IEEE Workshop on Signal Processing Advances in Wireless Communications*, New York, NY, USA, June 5-8, 2005; 260–264.
10. Brown III DR, Poor HV. Time-slotted round-trip carrier synchronization for distributed beamforming. *IEEE Transactions on Signal Processing* 2008; **56**: 5630–5643.
11. Dong L, Petropulu AP, Poor HV. Weighted cross-layer cooperative beamforming for wireless networks. *IEEE Transactions on Signal Processing* 2009; **57**: 3240–3252.
12. Zheng G, Wong K-K, Paulraj A, Ottersten B. Collaborative-relay beamforming with perfect CSI: optimum and distributed implementation. *IEEE Signal Processing Letters* 2009; **16**: 257–260.
13. Zarifi K, Zaidi S, Affes S, Ghraryeb A. A distributed amplify-and-forward beamforming technique in wireless sensor networks. *IEEE Transactions on Signal Processing* 2011; **59**: 3657–3674.
14. Zarifi K, Affes S, Ghraryeb A. Collaborative null-steering beamforming for uniformly distributed wireless sensor networks. *IEEE Transactions on Signal Processing* 2010; **58**: 1889–1903.
15. Astély D, Ottersten B. The effects of local scattering on direction of arrival estimation with MUSIC. *IEEE Transactions on Signal Processing* 1999; **47**: 3220–3234.
16. Amar A. The effect of local scattering on the gain and beamwidth of a collaborative beampattern for wireless sensor networks. *IEEE Transactions on Wireless Communications* 2010; **9**: 2730–2736.
17. Souden M, Affes S, Benesty J. A two-stage approach to estimate the angles of arrival and the angular spreads of locally scattered sources. *IEEE Transactions on Signal Processing* 2008; **56**: 1968–1983.
18. Bengtsson M, Ottersten B. Low-complexity estimators for distributed sources. *IEEE Transactions on Signal Processing* 2000; **48**: 2185–2194.
19. Jing Y, Jafarkhani H. Network beamforming using relays with perfect channel information. *IEEE Transactions on Information Theory* 2009; **55**: 2499–2517.
20. Zhao Y, Adve R, Lim T. Improving amplify-and-forward relay networks: optimal power allocation versus selection. *IEEE Transactions on Wireless Communications* 2007; **6**: 3114–3123.
21. Yi Z, Kim I. Joint optimization of relay-precoders and decoders with partial channel side information in cooperative networks. *IEEE Journal on Selected Areas in Communications* 2007; **25**: 447–458.
22. Seddik K, Sadek A, Su W, Liu K. Outage analysis and optimal power allocation for multi-node relay networks. *IEEE Signal Processing Letters* 2007; **14**: 377–380.
23. Farhadi G, Beaulieu NC. Low complexity receivers for coherent amplify-and-forward cooperative systems. *IEEE Transactions on Communications* 2010; **58**: 3001–3010.
24. Zaidi S, Affes S. Distributed collaborative beamforming with minimum overhead for local scattering environments, In *Proceedings of IEEE International Wireless Communications and Mobile Computing Conference (IWCMC'2012)*, Cyprus, August 27–31, 2012; 1–7. Invited Paper.
25. Zaidi S, Affes S. Distributed collaborative beamforming in presence of local scattering. submitted to *IEEE Transactions on Signal Processing*.

26. Affes S, Mermelstein P. Adaptive space–time processing for wireless CDMA. In *Adaptive Signal Processing: Application to Real-World Problems*, Benesty J, Huang AH (eds), Chap. 10. Springer: Berlin, Germany, 2003; 283–321.
27. Oppenheim AV, Schaffer RW, Buck JR. *Discrete-Time Signal Processing*, 2nd edition. Prentice Hall: New Jersey, USA, 1999.
28. Bellili F, Hassen SB, Affes S, Stephenne A. Cramer–Rao lower bounds of DOA estimates from square QAM-modulated signals. *IEEE Transactions on Signal Processing* 2011; **59**: 1675–1685.
29. Simon MK, Alouini M-S. *Digital Communications over Fading Channels*. Wiley: New York, USA, 2000.
30. Sanayei S, Nosratinia A. Opportunistic beamforming with limited feedback. *IEEE Transactions on Wireless Communications* 2007; **6**(8): 2765–2771.

AUTHORS' BIOGRAPHIES



Slim Zaidi received the BEng degree in Telecommunications with the highest honors from the National Engineering School of Tunis, Tunisia, in 2008 and the MSc degree from INRS-EMT, Université du Québec, Montreal, Quebec, Canada, in 2010. He is currently pursuing the PhD degree at INRS-EMT. His research interests include statistical signal and array processing, MIMO, cooperative communications, and wireless sensor networks. He acts regularly as a reviewer for many international scientific journals and conferences. Mr. Zaidi is the recipient of the National Grant of Excellence from the Tunisian Government.



Sofiene Affes (S'94-M'95-SM'04) received the Diplôme d'Ingénieur degree in telecommunications in 1992 and the PhD degree with honors in signal processing in 1995 both from the École Nationale Supérieure des Télécommunications (ENST), Paris, France. He has been with INRS-EMT, University of Quebec, Montreal, QC, Canada, as a Research Associate from 1995 until 1997, as an Assistant Professor until 2000, and then as an Associate Professor until 2009. Currently, he is a Full Professor in the Wireless Communications Group. His research interests are in wireless communications, statistical signal and array processing, adaptive space–time processing, cooperative communications and MIMO. From 1998 to 2002, he has been leading the radio design and signal processing activities of the Bell/Nortel/NSERC Industrial Research Chair in Personal Communications at INRS-EMT, Montreal, QC, Canada. From 2004 to 2011, he has been actively involved in major projects in wireless of PROMPT (Partnerships for Research on Microelectronics, Photonics and Telecommunications).

Prof. Affes was the co-recipient of the 2002 Prize for Research Excellence of INRS and a Discovery Accelerator Supplement Award from NSERC (Natural Sciences and Engineering Research Council of Canada) from 2008 to 2011. He currently holds a Canada Research Chair in Wireless Communications. In 2006, he served as a General Co-Chair of the IEEE Vehicular Technology Conference (VTC) 2006—Fall, Montreal, QC, Canada. In 2008, he received from the IEEE Vehicular Technology Society the IEEE VTC Chair Recognition Award for exemplary contributions to the success of IEEE VTC. He currently acts as a member of the Editorial Board of the *IEEE Transactions on Communications*, the *IEEE Transactions on Signal Processing*, the *IEEE Transactions on Wireless Communications*, and the *Wiley Journal on Wireless Communications and Mobile Computing*.